Catalysis Today 387 (2022) 12–22

Contents lists available at ScienceDirect

Catalysis Today

journal homepage: www.elsevier.com/locate/cattod

Promoter effect on the reduction behavior of wuestite-based catalysts for ammonia synthesis

Jan Folke [a,1], Kassiogé Dembélé [b,1], Frank Girgsdies [b], Huiqing Song [a], Rene Eckert [c], Stephan Reitmeier [c], Andreas Reitzmann [c], Robert Schlögl [a,b], Thomas Lunkenbein [b,*], Holger Ruland [a,*]

[a] Max Planck Institute for Chemical Energy Conversion, Department Heterogeneous Reactions, Stiftstraße 34-36, 45470, Mülheim an der Ruhr, Germany
[b] Fritz Haber Institute of the Max Planck Society, Department of Inorganic Chemistry, Faradayweg 4-6, 14195, Berlin, Germany
[c] Clariant Produkte (Deutschland) GmbH, Heufeld, Germany

ARTICLE INFO

Keywords:
Ammonia synthesis
Iron catalyst
Wuestite
Disproportionation
Quasi in situ characterization
Electron microscopy

ABSTRACT

Ammonia synthesis remains one of the most important catalytic processes since it enables efficient hydrogen storage and provides the basis for the production of fertilizers. Herein, complementary bulk and local analytical techniques were combined to investigate the effect of selected promoters (Al, K, Ca) on the reduction of wuestite into α-iron and their catalytic performance for ammonia synthesis. The use of promoters appears to have a positive effect on the wuestite-derived catalyst in ammonia synthesis. The promoters seemingly act as a binder for wuestite grains and impede the reduction and disproportionation events of wuestite precursors resulting in an increased catalytic performance. This effect is associated with an increase of surface area and mesoporosity. The study delivers new insights into the interplay of structure and promoters in wuestite-based catalysts.

1. Introduction

In the past centuries, human society has made tremendous technological and economical progress, which were accompanied by the rapid growth in world population [1]. The resulting challenge of fulfilling the increasing demand in food supply has always been a universal concern. As an efficient solution to this problem, intensive agriculture strongly relies on the industrial manufacturing of synthetic fertilizers, which require a large-scale supply of ammonia as feedstock. Fritz Haber [2–4] demonstrated the possibility of a catalyzed synthesis of ammonia from hydrogen and nitrogen under high temperature and pressure. Later Carl Bosch realized the industrial scale production of ammonia from its elements through the Haber–Bosch process [5,6].

Although many catalyst systems have been proven to be active for ammonia synthesis [7,8], only two of them showed a potential high enough for application in the industrial production of ammonia. One of these catalyst systems is the promoted Ru-based catalyst supported on carbon materials [9–11] or metal oxides [12–14]. However, the high manufacturing costs make Ru-based catalysts hard to compete with the other catalyst system [15,16], i.e. the industrially widely applied iron catalyst found by Alwin Mittasch. The catalyst precursor of the iron-based catalysts is routinely prepared by fusing iron oxides with other oxide additives consisting of "structural" promoters like Al_2O_3 and CaO, and "electronic" promoters like K_2O [17–20]. Prior to ammonia synthesis, the fused iron oxide, which contains additional oxide promoters, is activated by a multistep-reduction process in a H_2/N_2 mixture [21–23]. The iron oxide phase in the catalyst precursor has proven to be a crucial factor that influences the phase composition and the morphology of the reduced catalyst and determines the performance of the catalyst in ammonia synthesis [24,25]. Besides the conventional fused magnetite, wuestite has shown promising potential as an alternative catalyst precursor [25–28]. In the late 1980s, Liu et al. [27, 29–32] have reported that catalysts based on non-stoichiometric wuestite $Fe_{1-x}O$ as precursor show superior activity in ammonia synthesis compared to the magnetite-based catalysts. Please note, that although magnetite and wuestite are the typical industrial oxide precursors for Fe-based ammonia synthesis catalysts, Fe_2O_3-derived ammonia synthesis catalysts are widely applied in academic research [33–35].

In addition to the iron oxide precursor, the oxide promoters also play a decisive role not only in the formation of the active catalyst but also on

* Corresponding authors.
E-mail addresses: lunkenbein@fhi-berlin.mpg.de (T. Lunkenbein), holger.ruland@cec.mpg.de (H. Ruland).
[1] These authors contributed equally to this work.

https://doi.org/10.1016/j.cattod.2021.03.013
Received 29 November 2020; Received in revised form 3 March 2021; Accepted 7 March 2021
Available online 23 March 2021

the performance. Alumina is considered as one of the important structural promoters for ammonia synthesis catalyst [18,36]. For magnetite-based catalysts it is reported, that alumina is present in the reduced catalyst in the form of a thin Al_2O_3 layer [37,38] on the surface or segregated as both, $FeAl_2O_4$ and Al_2O_3 [39]. The presence of alumina or/and a Fe-Al solid solution [40] can prevent the activated iron from sintering, which would otherwise lead to the formation of larger crystals [18]. In the wuestite precursor, $FeAl_2O_4$ can also be formed via the solid reaction between FeO and Al_2O_3 [41]. However, due to the different crystal structure of FeO and $FeAl_2O_4$, the distribution of Al_2O_3 in the wuestite precursor is not as uniform as in magnetite precursors [25]. Consequently, it is assumed that alumina is not the only structural promoter and other oxide promoters such as SiO_2 and ZrO_2 are required [25]. Nevertheless, for wuestite-based precursor alumina is believed to participate in the restructuring of the surface of the reduced catalyst [25,42,43]. CaO is another structural promoter for catalysts based on magnetite as precursor [44,45]. In the reduced catalyst CaO segregates to the space between the Fe crystallites [46,47]. Furthermore, CaO increases the surface area and activity of the activated catalyst as well as promotes its resistance against impurities in the reactant gas [20]. For the wuestite precursor, CaO additionally inhibits the disproportionation reaction at low temperature of $Fe_{1-x}O$ which would form magnetite and metallic iron [25].

Besides the structural promoters, K_2O is the most important electronic promoter for ammonia synthesis catalysts based on both, magnetite or wuestite precursors [18,25]. Here, an enrichment of potassium on the surface during the reduction of the iron oxide precursors is taking place [25,46,48]. K_2O is hydrolyzed to strongly basic potassium hydroxide during the reduction, which enables the formation of amphoteric metal oxohydroxides with alumina and iron oxide [20]. The basic iron oxides act as a binder to the other oxide promoters as well as positively influence the reduction kinetics. In the activated catalyst K exists in the form of anhydrous KOH rather than a metallic adsorbate [20]. The promoting effect is attributed to the ability of the active anhydrous KOH species to enhance the dissociative adsorption energy of nitrogen, which is described as rate determining step of ammonia synthesis [20,49]. Furthermore, the basic KOH species reduces the adsorption energy of ammonia and, therefore, prevents the catalyst from self-poisoning caused by adsorption of the formed ammonia, especially at high reaction pressures.

In the present work, we focus on wuestite-based ammonia synthesis catalysts. To investigate the effect of different promoters on the performance of the catalyst, a series of wuestite-based catalysts containing different oxide promoters were synthesized, characterized and tested in ammonia synthesis. An industrial wuestite-based catalyst was used as reference. As we will show, disproportionation is the dominant chemical feature during the reductive activation at lower pressures and it can be strongly influenced by the use of promoters. Furthermore, the promoters as well as elevated pressure let all reductive events collapse into one reduction process that retains the phase disposition generated during fusion. This allows for the complete reduction of wuestite and the formation of "ammonia iron" below 500 °C.

2. Materials and methods

2.1. Synthesis of the precursor materials

The catalyst samples (Table 1) were prepared according to the recipe of the applied industrial catalyst in a lab-scale electric arc furnace. Raw materials were mixed together as fine powders, and the mixture was placed inside a melting pot. The furnace chamber was evacuated and the synthetic air pressure was set to the desired value. A voltage was applied, creating an electric arc. When the melting process was finished, the melt was cooled down and crushed by jaw crusher. Finally, the granules were sieved in order to obtain the desired size fraction.

Table 1
Composition of $Fe_{1-x}O$-based precursors.

Sample name	Promotors
FeO-01	none
FeO-02	K, Al
FeO-03	K, Al, Ca
FeO-04	multipromoted (industrial)

2.2. Catalyst characterization

For the TEM investigation, the wuestite grains were crushed and the resulting powders were dispersed in ultrapure ethanol and sonicated for 5 min. The experiments were performed with a transmission electron microscope (TEM) JEOL ARM 200 F operating at 200 kV, equipped with a double spherical aberration correctors, and GATAN Oneview and Orius cameras. For scanning TEM (STEM) studies, a high-angle annular dark-field (HAADF) detector was used, which maximized the collection of incoherent scattered electrons.

SEM investigations were conducted using Hitachi microscope, operating at 15 kV, and which is equipped with a secondary ion and electron detectors.

The BET surface areas and BJH pore size distributions were determined by measuring N_2-physisorption isotherms at −196 °C with a Quantachrome QUADRASORB evo MP set-up. For regular measurements of the air-stable precursors the sample surfaces were cleaned from water and other potential adsorbates by degassing them at 100 °C for 12 h in vacuum. The air sensitive catalysts after reduction were transferred without air contact and directly measured without any thermal pretreatment. BET surface areas were calculated from data collected in a p/p_0 range between 0.05 and 0.3. Adsorption and desorption isotherm were measured at a p/p_0 range between 0.05 and 0.95 and used for the determination of BJH pore size distributions.

The quasi in situ XRD data were collected in Bragg-Brentano geometry using a STOE Theta/theta X-ray diffractometer ($CuK_{\alpha 1+2}$ radiation, secondary graphite monochromator, scintillation counter) equipped with an Anton Paar XRK 900 in situ reactor chamber. The samples were reduced in the in situ chamber with a heating rate of 3 °C min^{-1} until the desired target temperature was reached, followed by rapid cooling (20 °C min^{-1}) and XRD measurement at 25 °C. Subsequently, the sample was heated again with 20 °C min^{-1} until reaching the previous target temperature, where the original TPR ramp of 3 K min^{-1} was resumed until the final reduction temperature of 850 °C was reached. The gas feed was mixed by means of Bronkhorst mass flow controllers, using 20 % H_2 in helium at a total flow rate of 100 N mL min^{-1}. The effluent gas composition was monitored with a Pfeiffer OmniStar quadrupole mass spectrometer. Ex situ XRD measurements of *post mortem* samples were performed in Bragg-Brentano geometry on a Bruker AXS D8 Advance II theta/theta diffractometer, using Ni filtered $CuK_{\alpha 1+2}$ radiation and a position sensitive energy dispersive LynxEye silicon strip detector. The diffraction patterns were analyzed by whole powder pattern fitting using the TOPAS software (version 5, ©1999−2014 Bruker AXS).

Temperature-programmed reduction (TPR) experiments were performed in a custom-designed set-up equipped with stainless-steel tubes, a fixed bed reactor (quartz glass, U-tube) and an on-line thermal conductivity detector (TCD) for monitoring the H_2 consumption. The TCD (Emerson X-stream) was calibrated by reducing a known amount of CuO. A molecular sieve containing tube was installed ahead of the detector as water trap.

For a measurement 100 mg of catalyst precursor (particle fraction 250−425 µm) were reduced by heating it to 900 °C in a total gas flow of 75 N mL min^{-1} (20 % H_2, 80 % Ar) applying a linear heating rate of 3 °C min^{-1}. The Monti-Baker criterion was in a range of 100–125 depending on the sample [50]. The Mallet-Caballero criterion was in a range of 5–6.5 K depending on the sample [51].

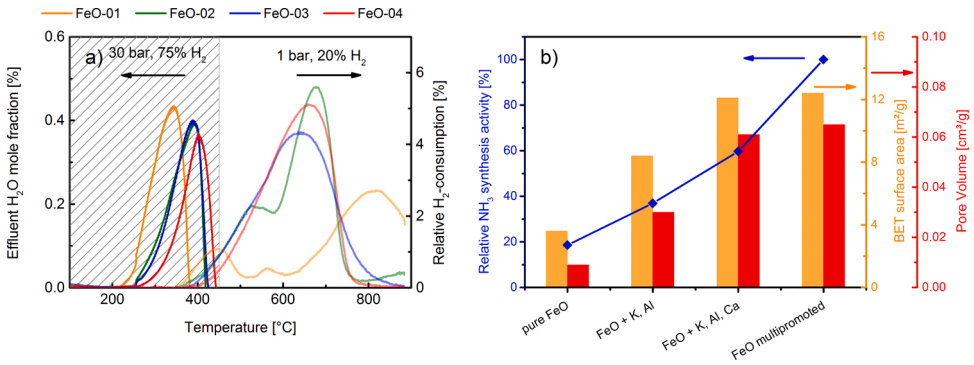

Fig. 1. a) H_2 consumption/H_2O formation during the reduction of the precursors at 30 bar and at 1 bar. b) Relative NH_3 synthesis activity at 400 °C and 90 bar normalized to the multipromoted industrial catalyst compared to their BET surface area and pore volume after catalytic testing.

2.3. Catalytic testing

The ammonia synthesis tests were conducted in a commercial all stainless-steel flow set-up (Integrated Lab Solutions Gmbh) equipped with a guard reactor, a synthesis reactor, and an on-line IR-detector for NH_3 and H_2O (Emerson X-stream) for quantitative product gas analysis. For a detailed description of the set-up see [52].

For a measurement 3 g of Fe-based precursor (particle fraction 425−560 µm) were diluted with 3.9 g SiC (average particle size 154 µm). The catalyst bed was placed in the synthesis reactor between pure SiC and held in position by glass wool plugs at the entrance and exhaust of the reactor. After intensive purging of the reactor until water content was stable at almost zero, the sample was reduced by heating it in a gas flow of 858 N mL min^{-1} (75 % H_2, 25 % N_2) with a temperature program up to 500 °C at an elevated pressure of 30 bar. The precursor was reduced in three temperature steps with different heating rates: from room temperature to 250 °C with 1.2 °C min^{-1}, 250−400 °C with 0.3 °C min^{-1} and 400−500 °C with 0.2 °C min^{-1}. Afterwards, the conditions were kept constant for ca. 4.5 h. In total the reduction procedure took 24 h.

For catalytic testing, the temperature was kept at 500 °C while the total gas flow was adjusted to 357 N mL min^{-1} (75 % H_2, 25 % N_2). The pressure was increased from 30 bar up to 90 bar in three steps of 20 bar. Each step was performed with a pressure ramp of 1 bar min^{-1} (1 h per step) and after reaching the elevated pressure it was kept constant for 40 min before starting the next step. After reaching 90 bar, the temperature was reduced to 400 °C with a rate of 1 °C min^{-1} and kept constant for 22 h. Afterwards the catalyst was heated again with 1 °C min^{-1} to 500 °C and measured for 14 h before cooling it back to 400 °C and measuring it for 22 h. This was repeated in total two times. At the end of the measurement the pressure was released and the catalyst was cooled down to room temperature, while the reactor was flushed with nitrogen. The tested sample was removed inside of a glovebox to allow further characterization of the catalyst in a reduced form. The activity of the catalysts is given as relative NH_3 synthesis activity, where the effluent mole fraction of NH_3 of the different catalysts was normalized to the initial effluent mole fraction of NH_3 of the industrial catalyst FeO-04.

3. Results and discussion

3.1. Reduction behavior/Catalytic activity

Four different $Fe_{1-x}O$-based precursors were investigated (Table 1) including three laboratory produced samples (FeO-01, FeO-02, FeO-03) and one industrially applied catalyst (FeO-04). The samples differ in their degree of promotion (Table 1). One laboratory sample (FeO-01) is unpromoted. FeO-02 is promoted with K and Al which reflect the most common promotors for all Fe-based ammonia synthesis catalysts [18]. FeO-03 has the same K and Al content as FeO-02 and is additionally doped with Ca as it is known to be one of the most important promoters for wuestite-based precursors [25]. The industrial FeO-based catalyst (FeO-04) contains a package of different promoters that are present in different amounts. The amounts of K, Al and Ca in FeO-04 are similar to FeO-03.

The precursors were activated by a reductive pretreatment as described in the experimental section to form the actual catalyst. The reduction of the precursors is accompanied by water formation and initiates the production of ammonia (Figure S1). Following the reductive activation, the catalytic activity towards ammonia synthesis was measured at a pressure of 90 bar at two different temperatures (400 °C and 500 °C) (Figure S2).

The reduction behavior of the $Fe_{1-x}O$ precursors varies strongly with the applied reduction conditions (Fig. 1a). Under the pressure of 30 bar the samples exhibit quite similar reduction profiles. The peak shape during reduction is asymmetric for all catalysts indicating overlaying reduction steps and/or higher order kinetics. Furthermore, the rate maximum is shifted to higher temperatures with increasing degree of promotion. Temperature programmed reduction (TPR) analysis of these catalysts at atmospheric pressure reveals kinetic resolution and a splitting of the reduction profile and for the catalysts with lower degree of promotion intermediate phases between reduction steps become stable. Due to the lower pressure and the lower H_2 amount in the gas phase the reduction potential is lower compared to the activation procedure at higher pressures as evidenced by the TPR measurements. In addition, the position of all reduction peaks is shifted to higher temperatures at lower hydrogen partial and total pressures. Although for pure wuestite only one reduction signal would be expected ($Fe_{1-x}O \rightarrow Fe$), the reduction profile of the unpromoted sample FeO-01 is split into three overlapping peaks. This arises from the consecutive reduction of wuestite and the disproportionation products. With increasing promotion the peak splitting decreases. While FeO-02 that is doped with K and Al shows two overlapping peaks, FeO-03 and FeO-04 exhibit only one visible reduction peak. This observation highlights that phase formation during reduction is strongly affected by the promoters acting on the catalysts synthesis as well as on the ammonia synthesis.

As expected, the comparison of the catalytic activity of the samples that is presented in Fig. 1b displays an enhancement of the activity with an increasing degree of promotion. The addition of K and Al (FeO-02) almost doubles the activity of the wuestite-based catalyst in comparison to the unpromoted sample (FeO-01). A further significant activity boost is achieved by the additional presence of Ca (FeO-03), which leads to an even three times higher activity compared to the unpromoted sample. With the addition of several different promoters the multi-promoted industrial catalyst (FeO-04) exhibits by far the highest activity and still leaves a significant gap to the sample with 3 promoters (FeO-03). The massive influence of promotion is especially visible by comparing the multi-promoted industrial catalyst (FeO-04) to the unpromoted sample (FeO-01). The multi-promoted $Fe_{1-x}O$-based catalyst is more

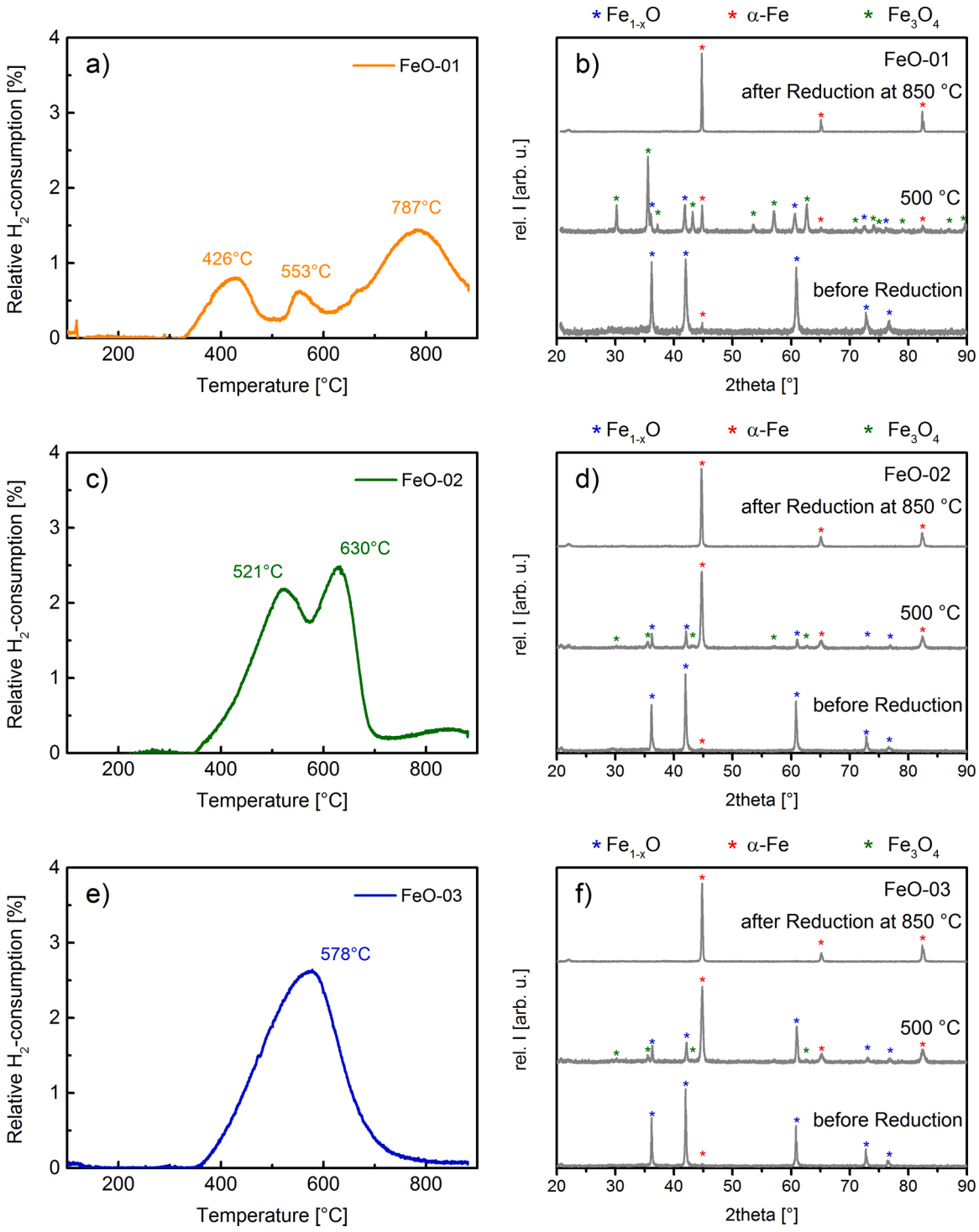

Fig. 2. Ambient pressure TPR profiles and quasi in situ XRDs of samples FeO-01 (a, b), FeO-02 (c, d) and FeO-03 (e, f).

than 5 times as active as the unpromoted analogue.

A major contribution to this increase in activity can be assigned to structural promotion as can be seen by the BET surface areas and mesoporous pore volumes of the reduced and tested catalysts (Fig. 1b, Table S1). The addition of K and Al (FeO-02) and the subsequent introduction of Ca (FeO-03) leads to an increasing surface area and pore volume quite comparable to the increase of the overall catalytic activity. It should be noted that this behavior does not exclude an influence of other promoting effects like the improvement of the reaction kinetics, where K is known to be important. In general, Al and Ca are known as structural promoters, which preserve the Fe nanostructures from sintering [27,32]. Furthermore, they cause an increase of the surface area of the catalyst and, therefore, an increase of the total number of active centers. By comparing the BJH pore size distribution of the samples after ammonia synthesis the difference in the effect of structural promotion becomes visible (Figure S3). While FeO-01 exhibits only little mesoporosity the addition of K and Al (FeO-02) leads to the formation of a small mesoporous pore volume with a broad pore size distribution. A significant effect can be seen by the addition of Ca (FeO-03). A clear mesoporous structure can be observed with a defined maximum

Table 2
Precursor composition during the quasi in situ XRD before, at 500 °C and after reduction estimated by quantitative Rietveld analysis.

Sample	Phase	Before Reduction	After Reduction to 500 °C	After Reduction at 850 °C
FeO-01	$Fe_{1-x}O$ [wt-%]	99	29	–
	Fe_3O_4 [wt-%]	–	64	–
	α-Fe [wt-%]	1	7	100
FeO-02	$Fe_{1-x}O$ [wt-%]	99	23	–
	Fe_3O_4 [wt-%]	–	13	–
	α-Fe [wt-%]	1	64	100
FeO-03	$Fe_{1-x}O$ [wt-%]	99	57	–
	Fe_3O_4 [wt-%]	–	7	–
	α-Fe [wt-%]	1	36	100

centered around 15 nm. The pore size distributions of FeO-03 and FeO-04 are almost identical. Thus, Ca seems to have a major role as a structural promoter and leads to the formation of a mesoporous network within high performance ammonia synthesis catalysts. Besides structural promoting, the addition of further promoters in FeO-04 may have a primary effect on the ammonia reaction kinetics, while the combination of K, Al and Ca in FeO-03 are believed to be the major constituents that lead to the total surface area and mesoporous nanostructure of the industrial catalyst.

3.2. Quasi in situ XRD of the reduction

As mentioned before the four samples vary in their reduction behavior during the TPR at 1 bar. In order to understand associated changes of the iron phases, XRD measurements were performed before the reduction, after the reduction and in the middle of the reduction process at 500 °C in a hydrogen-containing atmosphere. Due to the low time resolution (ca. 20 h per scan), all XRD measurements were performed at room temperature to avoid ongoing reduction of the sample during the data collection, which renders this technique quasi in situ. The intermediate target temperature of 500 °C was chosen according to the minima of the TPR profile of the sample FeO-01, while 850 °C was the maximum temperature accessible with the setup. At the minima of the TPR profile, the reduction rate is the lowest and thus the necessary interim cooling/re-heating phases should have the smallest possible impact on the reduction profile. Furthermore, it may be expected that potential intermediate phases have their maximum concentrations at these points. Although the minima are less resolved for FeO-02 or no TPR minima could be found for FeO-03, the same temperature program was applied to all samples for the sake of comparability.

Before reduction, the XRD patterns of all samples exhibit a distinct wuestite ($Fe_{1-x}O$) phase with a small amount of α-Fe, while after reduction only an α-Fe phase is present for all samples (Fig. 2). A difference for the samples can be observed with the XRD patterns in the middle of the reduction progress at 500 °C. It is possible to see the formation of a magnetite (Fe_3O_4) phase in different amounts for all samples before iron is fully reduced at higher temperatures. It should be noted that the XRD pattern of sample FeO-03 after reduction to 500 °C is peculiar in showing an unusually strong 220 reflection (60.5°) of the wuestite phase. Peak shape and broadening exclude the possibility of bad sampling statistics, which could cause significant intensity deviations in the case of highly crystalline phases. Furthermore, the cubic crystallographic symmetry and the lack of directing mechanical forces during the experiment rule out preferred orientation effects as a possible explanation. Thus, we interpret this surprising change of the relative intensities as a true structural effect. A Rietveld refinement was obtained after allowing the occupation of tetrahedral interstitial sites in the wuestite crystal structure by Fe atoms [53]. In the refined model, about one third of the iron atoms resided on the new tetrahedral positions, while the rest occupied the normal octahedral sites. Whether this unusual, modified wuestite phase is directly stabilized by the promoters in FeO-03, or whether it occurs generally as an intermediate during reduction and was only accumulated into noticeable amounts due to the delayed disproportionation/reduction kinetics, remains open.

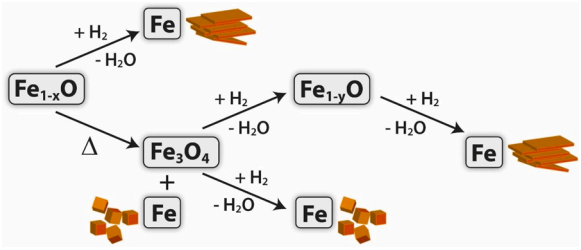

Fig. 3. Possible reduction pathways with disproportionation of $Fe_{1-x}O$.

The formation of magnetite is caused by thermal disproportionation of the wuestite into α-iron and magnetite. When the amounts of the different iron oxide phases are compared (Table 2) it can be seen that the unpromoted sample FeO-01 exhibits a much higher amount of magnetite at 500 °C compared to the two other promoted samples at this temperature. This shows that the promoters are stabilizing the metastable wuestite phase and inhibit thermal disproportionation (Fig. 2), i.e. minimizing the amount of magnetite at the final reduction temperature such that the individual events occur at lower temperature and coincide.

The thermal disproportionation can explain the peak splitting of the reduction peaks, which is strong in the unpromoted sample. Due to the disproportionation into α-Fe and Fe_3O_4 the precursor turns into phase mixtures of $Fe_{1-x}O$, α-Fe and Fe_3O_4. This leads to a reaction network during reductive activation (Fig. 3). Hence, parts of the $Fe_{1-x}O$ phase are directly reduced, while other parts of this phase disproportionate into iron and magnetite. The newly formed Fe_3O_4 is also reduced at higher temperatures compared to the original wuestite phase. It can be speculated that Fe_3O_4 forms during its reduction a new $Fe_{1-x}O$ phase as an intermediate step, which is subsequently reduced or disproportionated. It is further possible that $Fe_{1-x}O$ phases with different x values are formed. This could also explain the change of their reduction rate. At the applied higher temperatures all reactions can happen simultaneously as indicated by the overlaying TPR profiles.

Peak splitting in TPR decreases with increasing degree of promotion until only one reduction peak is present. However, disproportionation can still not be fully excluded as even the most promoted model sample FeO-03 still exhibits a detectable amount of magnetite as shown by the XRD patterns in Fig. 2f. Thus, the single reduction peak of the FeO-03 precursor can result from an overlap of different reduction events.

Please note, the quasi in situ XRD analysis was limited to a maximum measurement angle of 90° 2θ. Due to this limitation only three accessible reflections that can be assigned to bcc Fe could be obtained. The absence of further reflections has limited the peak profile analysis to consider only isotropic size broadening. Nonetheless, this analysis hints to a slight anisotropy in the peak profiles corresponding to α-Fe (Fig. 4) [54]. The peak width misfit is most pronounced for the 200 reflection. As opposed to the quasi in situ analysis, this effect of anisotropic peak broadening is more obvious in the diffraction patterns that were measured of all FeO catalysts after ammonia synthesis. However, these catalysts have been investigated ex situ. To illustrate the effect of anisotropic peak

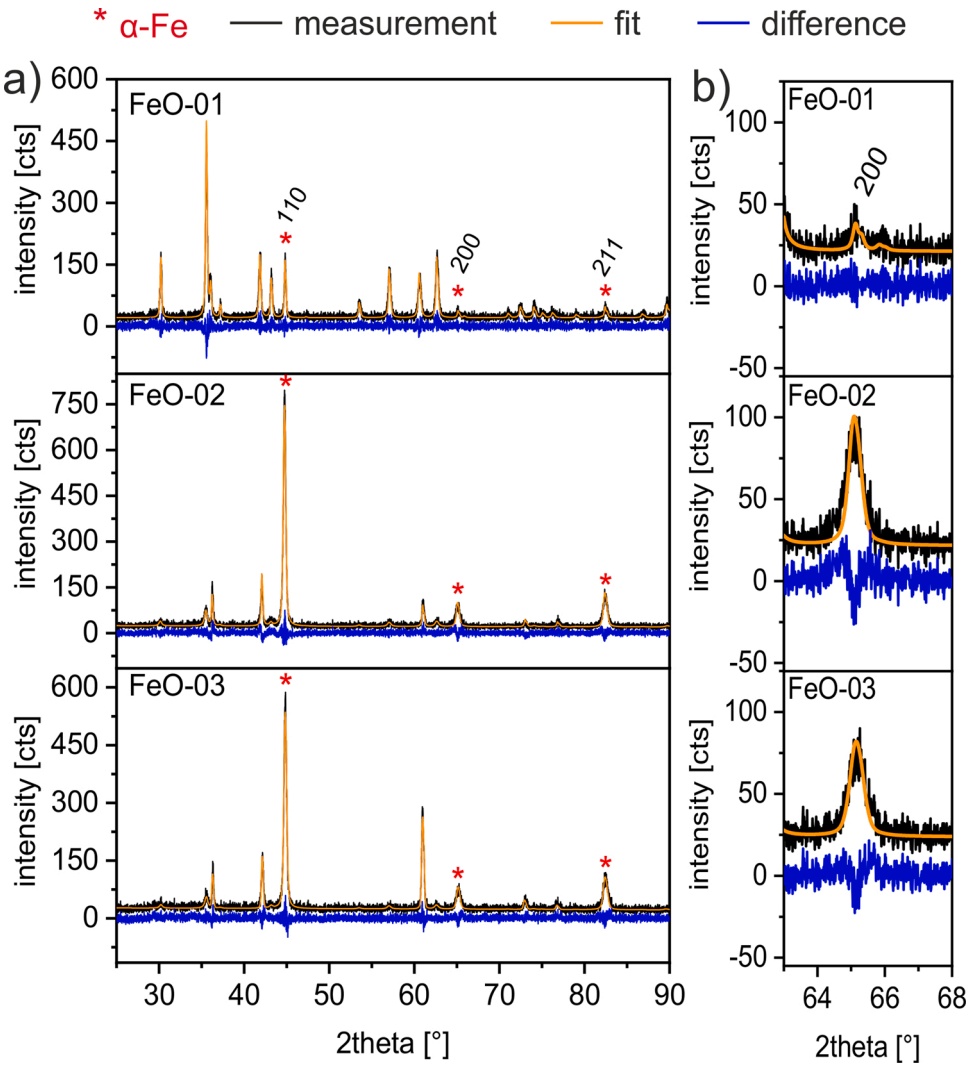

Fig. 4. Details of the XRD analysis of wuestite based ammonia synthesis catalysts. (a) Fitted quasi in situ XRD measurements of FeO-01, FeO-02, and FeO-03 after reduction at 500 °C and (b) enlarged XRD patterns of the 200 reflection. Only isotropic peak broadening was considered.

Table 3
Lattice parameters a and volume weighted mean domain sizes L_{Vol}-IB for the α-Fe phases of the investigated FeO samples at different temperatures. The numbers in parentheses represent estimated standard deviations (esd), referring to the last significant digit(s).

	Promoters	After reduction at 500 °C a [Å]	After reduction at 850 °C a [Å]	After reduction at 500 °C L_{Vol}-IB [nm]	After reduction at 850 °C L_{Vol}-IB [nm]
FeO-01	none	2.8672(2)	2.86747(6)	65(5)	520(30)
FeO-02	K, Al	2.86709(18)	2.86735(10)	27.4(7)	53.6(11)
FeO-03	K, Al, Ca	2.8697(2)	2.86752(8)	23.8(7)	55.3(11)

broadening, the XRD results of FeO-03 after ammonia synthesis are presented as a structural example in Figure S4a. The data was fitted with an isotropic profile in the absence of a crystal structure model. Furthermore, a fit that includes a crystal structure model (i.e. Rietveld refinement), reveals an additional mismatch of the calculated relative intensities for the spent FeO-03 catalysts (Figure S4b). Since the bcc crystal structure of α-Fe has no internal degrees of freedom, i.e. it accommodates only one atomic site that is fixed to a special position, except the thermal displacement parameter, this result can be taken as evidence that the real structure of the iron phase must be more complex than simple α-Fe. Phenomenologically, the observed intensity distribution could be approximated either by allowing the thermal displacement parameter to take physically implausible negative values or by assuming that additional electron density is residing on interstitial positions. It should be noted here that diffractometer misalignment or beam spill effects were explicitly ruled out as potential causes for the observed intensity mismatch.

From the applied Rietveld analysis of the experimental data of the wuestite precursors that have been measured by the quasi in situ XRD approach lattice parameters a and domain size values L_{Vol}-IB were extracted which are presented in Table 3. However, due to limitations to the isotropic fit model, these values should be interpreted only in terms of a trend rather than absolute values. The domain size values suggest that the addition of K, Al reduce sintering, while the addition of Ca seems to increase the Fe lattice parameter after reduction at 500 °C. It should be noted that the peculiarity of the lattice parameter occurs in the same scan as the "interstitial wuestite" phase occurred and vanishes with higher reduction temperatures.

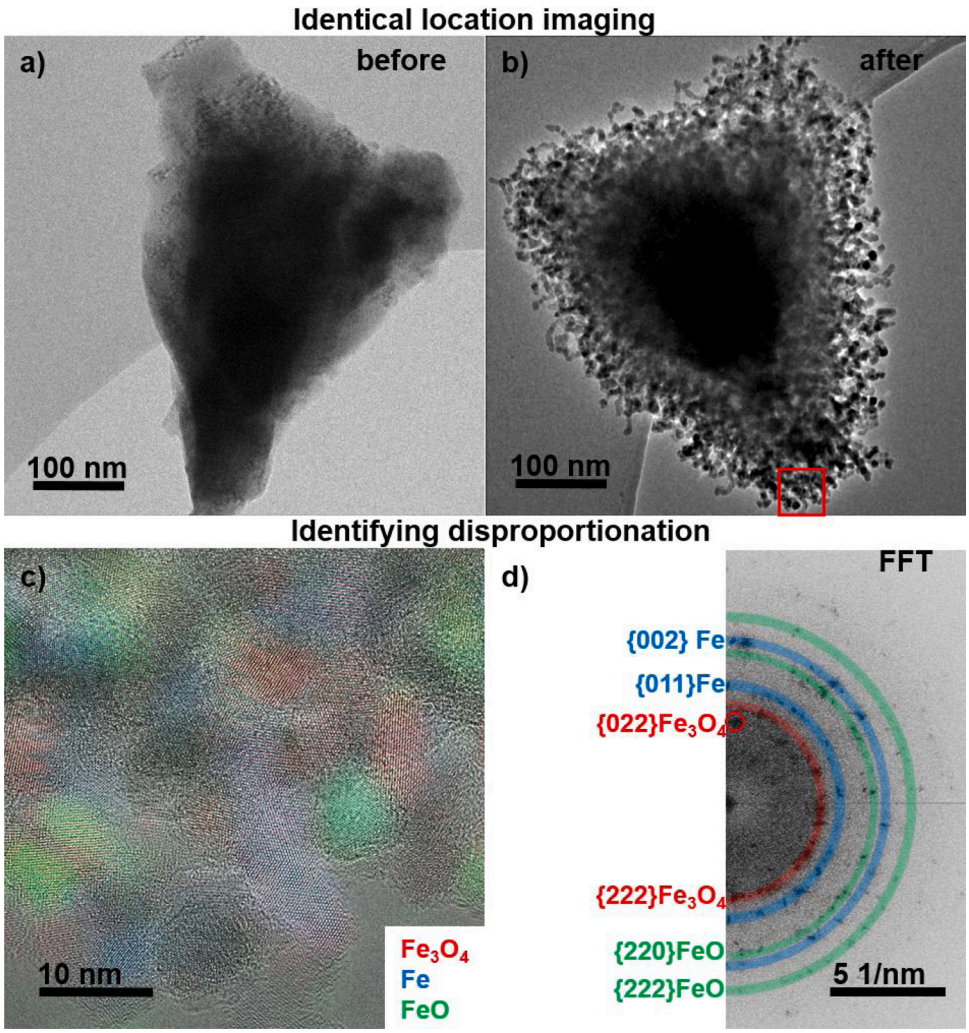

Fig. 5. TEM images of identical locations of FeO-03 before (a) and after (b) the quasi in situ experiment (H_2/Ar = 3/1, 10 bar, 365 °C) showing the reduction induced transformation of the nanostructure. False colored- HRTEM image (c) recorded at the edge of the particle (red square in b) and corresponding FFT (d), indicating the thermal disproportionation of wuestite into iron and magnetite.

These different possible reduction pathways render any detailed analysis difficult. While the formation of magnetite can only originate from the disproportionation of wuestite, the α-Fe can come from the disproportionation of wuestite as well as from the reduction of magnetite. In addition, it is possible that the full amount of all Fe phases cannot be detected by XRD due to the absence of translational symmetry or the formation of too small crystalline domains. For example, for sample FeO-01 (4 FeO → Fe_3O_4 + Fe) that exhibits a large amount of magnetite a α-Fe to magnetite weight-% ratio of 1–4 it could be stoichiometrically expected. However, the actual ratio is only around 1–9. This indicates that probably not all α-Fe in the sample is detected. Despite these uncertainties it is still possible to conclude on a few trends, in particular, when the amount of phases is strongly changing as it does for the aforementioned amount of magnetite. It is also possible to observe that the FeO-02 sample is at 500 °C more reduced indicated by a higher amount of α-Fe compared to FeO-03 sample. This can be explained by the presence of Ca in the FeO-03 sample, which slows down the reduction process of wuestite [55]. CaO crystallizes in the same crystal structure than wuestite and, therefore, it can be incorporated into the wuestite lattice [25]. This could form $Ca_xFe_{3-x}O_4$ solid solutions, which inhibits the disproportionation process. This is in agreement with the findings of Li et al. [55], who have shown the positive effect of CaO on thermal stability of wuestite structure under base pressure of 1.33 Pa. Meanwhile, the formation of $Ca_xFe_{3-x}O_4$ species will hinder the reduction rate in comparison to the wuestite precursor without Ca. A similar hindering effect of Ca on the magnetite-based precursor reduction has been reported by Liu et al. [32]. As the Ca content is sufficiently low the precipitation of the spinel phase could be avoided. It has been highlighted that phase purity of the oxide precursor is a necessary requirement for a good ammonia synthesis catalysts [25].

3.3. Quasi in situ TEM of the reduction

To investigate how the early stages of disproportionation influences the structure on the local scale transmission electron microscopy investigations were conducted. Transmission electron microscopy allows to investigate the morphology and structure of the catalysts at the (sub)-nanometric scale and is thus complementary to bulk averaging characterization techniques. In order to study the morphological and structural changes that occur during the reduction on the individual particles, quasi in situ TEM experiments were conducted [56,57]. This later allows to investigate catalyst particles before and after activation at elevated pressure and temperature, which are relevant for ammonia synthesis catalysts.

The reduction of the wuestite was first followed for the FeO-03 precursor to exemplify the presence of local disproportionation events for a fully promoted sample by submitting the sample to a H_2/Ar mixture of 3 to 1 at 10 bar and 365 °C. Fig. 5 shows typical and identical wuestite

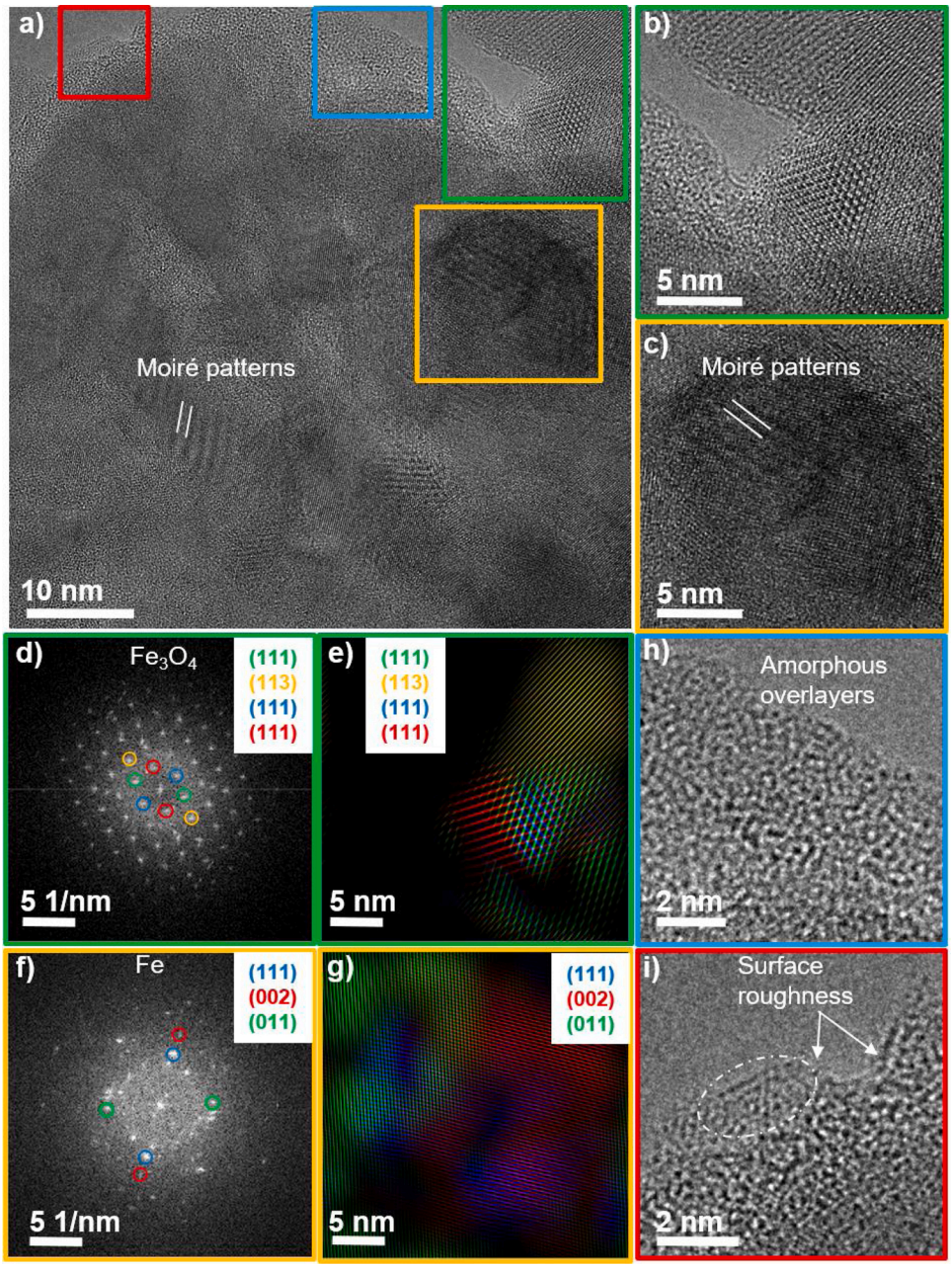

Fig. 6. HRTEM images (a) on FeO-03 after quasi in situ experiment at $H_2/Ar = 3/1$, 10 bar, 365 °C. Zoom into the areas framed by green (b), and orange rectangles (c); the corresponding FFT (d and f) analysis indicate the formation of magnetite; addition of inverse FFT (e and g) showing the position of individual reflections in the HRTEM images. The overlapping of lattice planes is noticed in (g) with the apparition of orange and violet colors. The HRTEM images focusing on blue and red rectangles indicates the presence of amorphous (h), short-range order (dashed ellipse) and surface roughness (i) on the overlayer of the agglomerate.

particles before (Fig. 5a) and after the quasi in situ experiment (Fig. 5b). Before quasi in situ activation (Fig. 5a), surface near diffraction contrast indicates the formation of defective structures within the particles which are characteristic of wuestite-type materials. After reductive treatment (Fig. 5b), a cracking of the identical particle occurred that can be best described by the formation of a hedgehog-like structure, which is accompanied by the formation of porosity and the outgrowth of multiple nanoplatelets [58,59]. High-resolution (HR)-TEM imaging and corresponding Fast-Fourier transform (FFT) analysis (Fig. 5c-d) of the nanoplatelets denote the growth of polycrystalline particles with a nanoparticular structure. After treatment at 365 °C the wuestite structure is still present in the sample. In addition, α-iron and magnetite are formed. Thus, this observation corroborates the thermal disproportionation in the early stage of the reduction process, as previously established by XRD and TPR even for the fully promoted samples.

Additional areas of the FeO-03 sample after reduction were investigated, which show the formation of complex structures and the local inhomogeneity of the sample. Fig. 6 presents one example of a detailed HRTEM analysis. Polycrystalline particles are observed including the presence of Fe_3O_4 (Fig. 6b–d) and Fe (Fig. 6e–g) phases. In addition, Moiré patterns (Fig. 6a and e) as a result of overlapping lattice planes indicate the presence of turbostratic disordered layers, which can also highlight the formation of defective phases. The complexity of the atomic structure is further corroborated by analyzing the surface layer of such a particular aggregate, including amorphous layers (Fig. 6h), short-range ordered surface structures (dashed ellipse in Fig. 6i) and surface roughness (Fig. 6i). The observation of amorphous and short-range ordered phase may also be in line with the missing Fe content calculated from Rietveld analyzed XRD patterns. Elemental analysis indicates that the promoters (Al, K, Ca) are in close contact with iron phases (Figure S5).

From the above results, it is apparent that the temperature of 365 °C is insufficient to fully reduce the wuestite precursor even at elevated pressure. In order to corroborate the TPR results showing that at

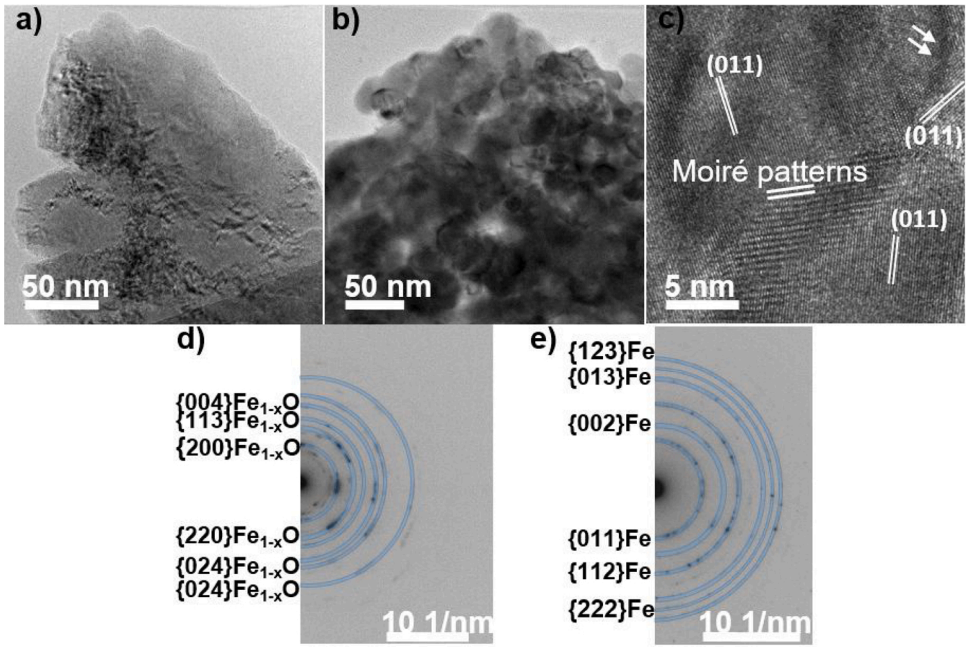

Fig. 7. TEM images on FeO-01 precursor before (a) and after quasi in situ TEM reduction (b-c) at $H_2/Ar = 3/1$, 10 bar, 470 °C; HRTEM images after reduction (c) showing α-Fe (011) planes of different crystals, Moiré patterns and strain (arrows); SAED analysis before (d) and after activation (e) indicating the reduction of wuestite into iron.

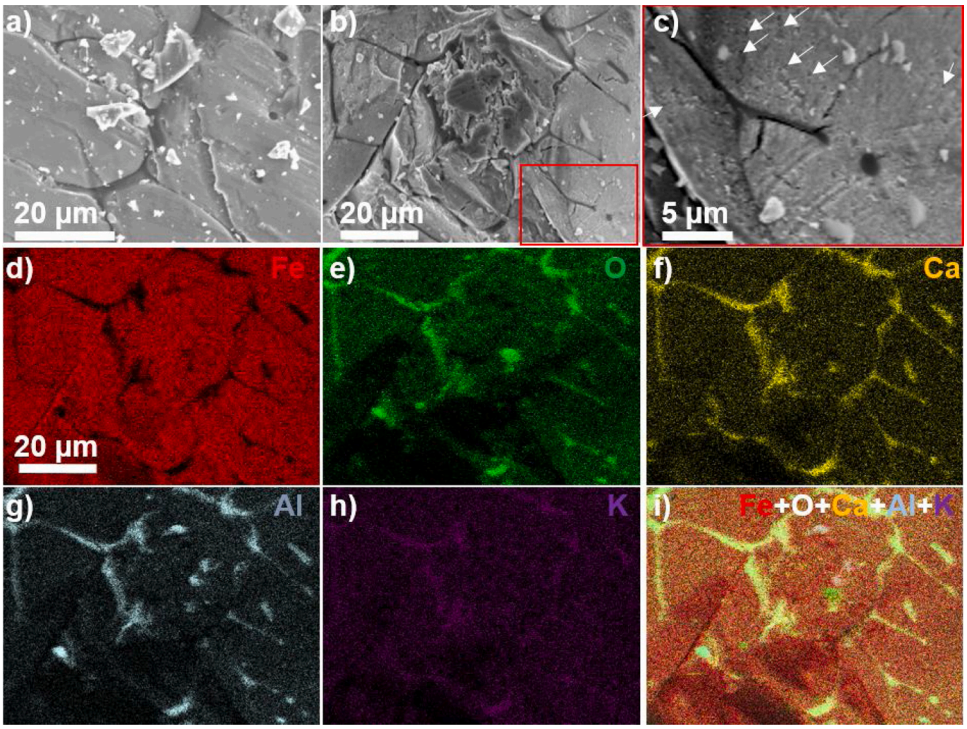

Fig. 8. SEM images on the FeO-03 sample before reduction (a) as well as after reduction and NH_3 synthesis (b). Zoom in of the grains (c) showing the presence of sponge-like structure (see white arrows); SEM-EDX mapping (d-f) on the FeO-03 after NH_3 synthesis, showing the presence of Fe, O and promoters (Al, K, Ca); Addition of SEM-EDX elemental maps (i).

elevated pressure and higher temperature (above 400 °C) also the unpromoted sample can be fully reduced quasi in situ investigations of FeO-01 were conducted. Fig. 7 shows TEM images on the FeO-01 sample before (Fig. 7a) and after (Fig. 7b) quasi in situ reduction experiment at 10 bar of H_2/N_2 (3/1) mixture at 470 °C showing that at elevated pressure the unpromoted sample is fully reduced even at the local scale. The wuestite precursor (Fig. 7a) indicates a particle-like morphology with a length of about 500 nm. Similar to the pristine FeO-03 sample, localized diffraction contrast is observed which is distributed all over the particle. After the exposure of the precursor to a H_2/N_2 (3/1) mixture at 10 bar and 470 °C (Fig. 7b), a drastic morphological change occurred which is expressed by the formation of elongated polycrystalline iron

phases. This is confirmed by HRTEM imaging (Fig. 7c), which shows the presence of (011) α-Fe planes of different crystals. The HRTEM also shows the formation of Moiré patterns between the agglomerates of particles, as a result of the interference of overlapping (011) lattice planes indicating thin layers. Furthermore, the particles exhibit a dark contrast (see arrows in the Fig. 7c), which is indicative of the formation of strains on the particles.

In addition, the structure of the sample before and after the quasi in situ reduction was investigated using selected area electron diffraction (SAED). Ring patterns were observed in both before (Fig. 7d) and after (Fig. 7e) quasi in situ reduction, indicating a polycrystalline structure with a small crystallite size. The analysis confirms that the full reduction of wuestite precursors to Fe occurs at elevated pressures even for the unpromoted sample at lower temperatures which corroborates the TPR results presented in Fig. 1a.

It should be noted that we have conducted similar reduction experiments for FeO-02 by quasi in situ TEM (see Figure S7). As demonstrated for FeO-01 (Fig. 7) the sample is reduced and similar morphological and structural features were detected.

3.4. SEM after NH_3 synthesis

Additionally, the microstructure of the FeO-03 sample before reduction (Fig. 8a) as well as after reduction and ammonia synthesis (Fig. 8b-c) was investigated by scanning electron microscopy (SEM). A complex microstructure is observed with the presence of different grain sizes (Fig. 8a). Furthermore, grain boundaries can be observed which indicate the presence of a defective structure. The bulk morphology of the wuestite precursor is similar to the one after ammonia synthesis. However, a sponge-like structure is formed with voids distributed all along (see areas highlighted by arrows in Fig. 8c). This is in line with the BJH results, which showed a clear mesoporous structure for the wuestite sample promoted with K, Al and Ca. This may be related to the reduction of the particles, which generates the porosity and increases the surface area of the particles as confirmed by the BET surface area.

In order to investigate the microstructure and chemical composition on the sponge-like structure formed after NH_3 synthesis, SEM-EDX mapping were conducted (Fig. 8d–I and Figure S6). The EDX mapping has revealed the presence mainly of Fe. However, O, Al, K, Ca were also detected, and are more concentrated into the grain boundaries. Similar localization of the promoters in the wuestite grains before reduction were observed (see Figure S8). Therefore, the promoters could act as binders between the larger grains and thus help to stabilize the sample morphology during the reduction/activation steps.

4. Conclusion

In summary, the reduction of wuestite-based precursors occurs in a complex reaction network involving reduction and disproportionation events. Our results show positive effects of K, Al and Ca as the main promoters on the performance and reduction behavior of wuestite-based ammonia synthesis catalysts. They have a significant influence on improving and stabilizing the catalyst nanostructure that is defined during the fusion and retained during the reduction of the precursors, whereas the promoters seem to be concentrated in the grain boundaries of the formed α-iron bulk crystals. Furthermore, they narrow the reduction and disproportionation events of metastable wuestite which allows a more direct reduction with less amounts of magnetite at the final activation temperature. The presented results support the formation of a structure of defective and disordered nanoplatelets within a mesoporous network as the origin of “ammonia iron” in comparison to bulk α-iron. This enhances by far the surface area of the catalyst. These global improvements from the promoters lead to a more active catalyst for ammonia synthesis. Especially Ca seems to play a major role on defining the reduction process and, therefore, also the mesoporous network and the surface area of the resulting catalyst. We note that the difference between normal iron and ammonia iron mostly occurs on a mesoscopic scale. Typical spectroscopies as Mössbauer or EXAFS would not detect such differences [60]. XRD is slightly sensitive in its line shapes [61] being peculiar in active catalysts. The information content of these anomalies precludes a distinction of mesoscopic defect from possibly present additional local defects for which TEM gave some hints.

CRediT authorship contribution statement

Jan Folke: Writing - original draft, Investigation, Validation, Formal analysis, Visualization. **Kassiogé Dembélé:** Writing - original draft, Investigation, Validation, Formal analysis, Visualization. **Frank Girgsdies:** Investigation, Formal analysis, Visualization, Writing - review & editing. **Huiqing Song:** Investigation, Validation, Formal analysis, Writing - original draft. **Rene Eckert:** Investigation, Writing - original draft, Writing - review & editing, Project administration. **Stephan Reitmeier:** Writing - review & editing, Resources, Supervision. **Andreas Reitzmann:** Writing - review & editing, Resources, Supervision. **Robert Schlögl:** Conceptualization, Methodology, Writing - review & editing, Resources, Supervision. **Thomas Lunkenbein:** Conceptualization, Methodology, Writing - original draft, Writing - review & editing. **Holger Ruland:** Conceptualization, Methodology, Writing - original draft, Writing - review & editing, Project administration.

Declaration of Competing Interest

The authors declare no conflict of interest.

Acknowledgement

The authors would like to thank the Max Planck Society for financial support. Furthermore, we thank Birgit Deckers for the graphical artwork.

Appendix A. Supplementary data

Supplementary material related to this article can be found, in the online version, at doi:https://doi.org/10.1016/j.cattod.2021.03.013.

References

[1] P. Gerland, A.E. Raftery, H. Ševčiková, N. Li, D. Gu, T. Spoorenberg, L. Alkema, B. K. Fosdick, J. Chunn, N. Lalic, G. Bay, T. Buettner, G.K. Heilig, J. Wilmoth, Science 346 (2014) 234.
[2] F. Haber, R. Le Rossignol, Z. Elektrochem. 14 (1908) 513.
[3] F. Haber, Z. Elektrochem. 16 (1910) 244.
[4] F. Haber, R. Le Rossignol, Z. Elektrochem. 19 (1914) 53.
[5] C. Bosch, Patent US1386760A (1912).
[6] C. Bosch, A. Mittasch, Patent US993144A (1911).
[7] J.R. Jennings, Catalytic Ammonia Synthesis, Plenum, New York, 1991.
[8] J. Humphreys, R. Lan, S. Tao, Adv. Energy Sustain. Res. 2 (2021), 2000043.
[9] Z. Zhong, K. Aika, J. Catal. 173 (1998) 535.
[10] K. Aika, H. Hori, A. Ozaki, J. Catal. 27 (1972) 424.
[11] Ch. Liang, Z. Li, J. Qiu, C. Li, J. Catal. 211 (2002) 278.
[12] J. Iwamoto, M. Itoh, Y. Kajita, M. Saito, K. Machida, Catal. Commun. 8 (2007) 941.
[13] P. Moggi, G. Albanesi, G. Predieri, G. Spoto, Appl. Catal. A: General 123 (1995) 145.
[14] H. Bielawa, O. Hinrichsen, A. Birkner, M. Muhler, Angew. Chem. Int. Ed 40 (2001) 1061.
[15] W. Rarogpilecka, E. Miskiewicz, D. Szmigiel, Z. Kowalczyk, J. Catal. 231 (2005) 11.
[16] Q.C. Xu, J.D. Lin, J. Li, X.Z. Fu, Z.W. Yang, W.M. Guo, D.W. Liao, J. Mol. Catal. A Chem. 259 (2006) 218.
[17] G. Ertl, D. Prigge, R. Schlögl, M. Weiss, J. Catal. 79 (1983) 359.
[18] R. Schlögl, in: G. Ertl, H. Knözinger, J. Weitkamp (Eds.), Handbook of Heterogeneous Catalysis, Wiley-VCH, Weinheim, 2008.
[19] H. Liu, Chin. J. Catal. 35 (2014) 1619.
[20] A. Nielsen, Ammonia Catalysis and Manufacture, Springer, Heidelberg, 1995.
[21] J. Schötze, W. Mahdi, B. Herzog, R. Schlögl, Top. Catal. 1 (1994) 195.
[22] W. Büchner, R. Schlibs, G. Winter, K.H. Büchel, Industrielle Anorganische Chemie, VCH, Weinheim, New York, 1986, p. 34.
[23] A. Nielsen, Catal. Rev. 23 (1981) 17.
[24] R. Schlögl, Angew. Chem. Int. Ed 42 (2003) 2004–2008.
[25] H. Liu, W. Han, Catal. Today 297 (2017) 276.

[26] N. Pernicone, F. Ferrero, I. Rossetti, L. Forni, P. Canton, P. Riello, G. Fagherazzi, M. Signoretto, F. Pinna, Appl. Catal. A: General 251 (2003) 121.
[27] H.Z. Liu, X.N. Li, Z.N. Hu, Appl. Catal. A: General 142 (1996) 209.
[28] W. Han, S. Huang, T. Cheng, H. Tang, Y. Li, H. Liu, Appl. Surf. Sci. 353 (2015) 17.
[29] H.Z. Liu, Z.N. Hu, X.N. Li, Y.Y. Li, Z.R. Jiang, J. Chem. Ind. Eng. 45 (1994) 385.
[30] H.Z. Liu, X.N. Li, Sci. China Chem. 38 (1995) 529.
[31] H.Z. Liu, X.N. Li, Ind. Eng. Chem. Res. 36 (1997) 335.
[32] H.Z. Liu, Ammonia Synthesis Catalysts Innovation and Practice, World Scientific and chemical industry press, Singapore, 2013, pp. 47–49.
[33] J. Humphreys, R. Lan, S. Chen, S. Tao, J. Mater. Chem. A 8 (2020) 16676.
[34] B. Cai, H. Liu, W. Han, Catalysts 10 (2020) 1027.
[35] J. Humphreys, R. Lan, S. Chen, M. Walker, Y. Han, S. Tao, Appl. Catal. B: Environmental 285 (2021), 119843.
[36] R. Krabetz, C. Peters, Angew. Chem. 77 (1965) 333.
[37] G. Ertl, N. Thiele, Appl. Surf. Sci. 3 (1979) 99.
[38] M. Weiss, G. Ertl, Stud. Surf. Sci. Catal. 11 (1982) 277.
[39] Cl. Peters, K. Schafer, R. Krabetz, Z. Elektrochem. 64 (1960) 1194.
[40] R. Hosemann, A. Preisinger, W. Vogel, Ber. Bunsenges. Phys. Chem 70 (1966) 796.
[41] M.J. Figurski, W. Arabczyk, Z. Lendzion-Bieluń, R.J. Kaleńczuk, S. Lenart, Appl. Catal. A: General 247 (2003) 9.
[42] A. Barański, A. Kotarba, J.M. Łagan, Appl. Catal. 71 (1991) L1.
[43] Z. Kowalczyk, S. Jodzis, J. Środa, R. Diduszko, E. Kowalczyk, Appl. Catal. A: General 87 (1992) 1.
[44] B. Wilk, R. Pelka, W. Arabczyk, J. Phys. Chem. C 121 (2017) 8548.
[45] M.E. Dry, J.A.K. du Plessis, G.M. Leuteritz, J. Catal. 6 (1966) 194.
[46] P.H. Emmett, S. Brunauer, J. Am. Chem. Soc. 56 (1934) 35.
[47] A. Nielsen, H. Bohlbro, J. Am. Chem. Soc. 74 (1952) 963.
[48] S. Brunauer, P.H. Emmett, J. Am. Chem. Soc. 62 (1940) 1732.
[49] D.R. Strongina, G.A. Somorjai, J. Catal. 109 (1988) 51.
[50] D.A.M. Monti, A. Baiker, J. Catal. 83 (1983) 323–335.
[51] P. Malet, A. Caballero, J. Chem. Soc. Faraday Trans. 1 (84) (1988) 2369–2375.
[52] J. Folke, H. Song, J. Schittkowski, R. Schlögl, H. Ruland, Chem. Ing. Tech. 92 (2020) 1567–1573.
[53] J.-R. Gavarria, C. Carel, Prog. Solid State Ch 53 (2019) 27.
[54] T. Kandemir, M.E. Schuster, A. Senyshyn, M. Behrens, R. Schlögl, Angew. Chem. Int. Ed 52 (2013) 12723–12726.
[55] X. Li, Y. Cen, H. Liu, Y. Xu, G. Lv, React. Kinet. Catal. Lett. 81 (2004) 313.
[56] L. Masliuk, M. Swoboda, G. Algara-Siller, R. Schlögl, T. Lunkenbein, Ultramicroscopy 195 (2018) 121.
[57] P.J. Kooyman, J.G. Buglass, H.R. Reinhoudt, A.D. van Langeveld, E.J.M. Hensen, H. W. Zandbergen, J.A.R. van Veen, J. Phys. Chem. B 106 (2002) 11795–11799.
[58] A. Barafiski, M. Lagan, A. Pattek, A. Reizer, Archiwum Hutnictwa 25 (1980) 143.
[59] A. Baranski, A. Kotarba, J.M. Lagan, A. Pattek-Janczyk, E. Pyrczak, A. Reizer, Appl. Catal. A: General 112 (1994) 13–36.
[60] W. Niemann, B.S. Clausen, H. Topsoe, Ber. Bunsenges. Phys. Chem 91 (1987) 1292.
[61] W. Vogel, J. Haase, R. Hosemannn, Z. Naturforschung 29a (1974) 1152–1158.